Rotational Effects on the Boundary-Layer Flow in Wind Turbines

Horia Dumitrescu* and Vladimir Cardos†
Institute of Statistics and Applied Mathematics, Ro 70700 Bucharest, Romania

I. Introduction

THE use of two-dimensional steady-state airfoil data in strip theory result in unsatisfactory predictions of wind turbine loads at high wind speeds and when operating in yaw. The maximum power for stall-regulated turbines is generally underpredicted with use of two-dimensional wind-tunnel data. To simulate correctly the loading and performance of a wind turbine operating in stall, it is clear that three-dimensional effects have to be included in aerodynamic calculations.

The rotational three-dimensional effects on the boundary layer and their consequences for wind turbine rotors have been studied both by the analysis of experiments[1,2] and by the use of a range of theoretical methods that investigate the steady flow on a rotating wind turbine blade.[3–5] Data from experiments show consistency in that a stall delay is found in all experiments for radial stations of the inboard part of the blade, typically around $r/R \leq 0.3$. Calculations with viscous/inviscid interaction and Navier–Stokes codes carried out both for rotating and nonrotating blades also show stall delay for small radius. The calculated pressure distributions for a rotating blade with a stall delay are qualitatively similar, and both methods show a triangular-type pressure distribution also found in measurements. This result indicates that the main cause for the stall delay and increased three-dimensional poststall coefficients is the effect of the rotation with Coriolis forces occurring in the separated three-dimensional boundary-layer flow. On the other hand, this explanation is opposite to that given by Wood,[6] who assigned the stall delay only to the pressure changes occurring in external flow.

It is believed, however, that beyond this physical reasoning, which is based largely on intuition, there must be a theoretical formulation that substantiates the distinct contributions of the two flows. In view of the rotational effects, the only difference between these two motions is the way the flow is being accelerated. This prompts us to reexamine the problem from the viewpoint of a moving reference frame.

II. Boundary-Layer Equations

We begin with Navier–Stokes equations written in terms of a coordinate system fixed to a body rotating at a steady rate $\boldsymbol{\Omega}(\mathrm{d}\boldsymbol{\Omega}/\mathrm{d}t = 0)$:

$$\nabla \boldsymbol{u} = 0 \tag{1}$$

$$\frac{1}{Ro}\frac{\partial \boldsymbol{u}}{\partial t} + (\boldsymbol{u}\cdot\nabla)\boldsymbol{u} = -\nabla p + \boldsymbol{F} + \frac{1}{Re}\nabla^2 \boldsymbol{u} \tag{2}$$

where $\boldsymbol{F}$ is the sum of various apparent bodies forces resulting from accelerations of the reference frame:

$$\boldsymbol{F} = -(1/Ro)[2\boldsymbol{\Omega}\times\boldsymbol{u} + (1/Ro)\boldsymbol{\Omega}\times(\boldsymbol{\Omega}\times\boldsymbol{r})]$$

The preceding equations have been nondimensionalized by taking the body length L, the dimensional rotary speed of the reference frame (the constant magnitude of $\boldsymbol{\Omega}$), and a typical velocity U_∞ as the proper length, time, and velocity scales, respectively. The two dimensionless parameters appearing in the equations are the Reynolds number $Re = U_\infty L/\nu$ and the Rossby number $Ro = U_\infty/\Omega L$, which expresses the ratio of inertial to Coriolis forces.

As in the conventional case, Prandtl's proposition of boundary-layer approximation can be equally applied to the present moving-body formulation. Let x and y be the coordinates measured along the body surface and z the coordinate normal to the wall. Following exactly the same argument as for the inertial case, one can still assume there exists a thin layer of thickness δ adjacent to the body within which the viscous effect is confined. Under these assumptions, the transverse velocity component w and the pressure variation Δp across the layer are of order δ, that is, $w \sim \mathcal{O}(\delta)$, and $\Delta p \sim \mathcal{O}(\delta)$, provided that all inertial accelerations in the apparent body-force term $\boldsymbol{F}$ are no greater than $\mathcal{O}(1)$. Thus, the continuity equation remains unchanged:

$$\frac{\partial u}{\partial x} + \frac{\partial v}{\partial y} + \frac{\partial w}{\partial z} = 0 \tag{3}$$

where u, v, and w are components of the velocity vector $\boldsymbol{u}$ along the coordinates x, y, and z, respectively. The momentum equations, after higher-order terms are dropped and the pressure gradient from the outer inviscid flow are replaced, become

$$\begin{aligned}
&\frac{1}{Ro}\frac{\partial u}{\partial t} + u\frac{\partial u}{\partial x} + v\frac{\partial u}{\partial y} + w\frac{\partial u}{\partial z} \\
&\quad = \frac{1}{Ro}\frac{\partial U}{\partial t} + U\frac{\partial U}{\partial x} + V\frac{\partial U}{\partial y} + F_x' + \frac{1}{Re}\frac{\partial^2 u}{\partial z^2} \\
&\frac{1}{Ro}\frac{\partial v}{\partial t} + u\frac{\partial v}{\partial x} + v\frac{\partial v}{\partial y} + w\frac{\partial v}{\partial z} \\
&\quad = \frac{1}{Ro}\frac{\partial V}{\partial t} + U\frac{\partial V}{\partial x} + V\frac{\partial V}{\partial y} + F_y' + \frac{1}{Re}\frac{\partial^2 v}{\partial z^2}
\end{aligned} \tag{4}$$

where U and V are components of the local free stream $\boldsymbol{U}$ tangent to the body surface and F_x' and F_y' are tangential components of the differential apparent body force $\boldsymbol{F}'$:

$$\boldsymbol{F}' = \boldsymbol{F}^{(\delta)} - \boldsymbol{F}^{(i)} = (2/Ro)\boldsymbol{\Omega}\times(\boldsymbol{U}-\boldsymbol{u}) \tag{5}$$

Equations (3) and (4) are the governing equations for three-dimensional boundary-layer flows as observed from an object rotating in space. The only extra term [Eq. (5)] in the tangential momentum equations represents the Coriolis effect arising from the component of the rigid-body rotation normal to the local surface.

For two-dimensional plane inviscid motion, such as a rotation blade, the rotation vector is perpendicular to the plane, and evaluation of the boundary layer is then determined solely by the prescribed effective pressure gradient:

$$-\left.\frac{\partial p}{\partial x}\right|_{\text{eff}} \equiv \frac{1}{Ro}\frac{\partial U}{\partial t} + U\frac{\partial U}{\partial x} = -\frac{\partial p}{\partial x} + F_x^{(i)} = -\frac{\partial}{\partial x}\left(p - \frac{1}{Ro^2}\frac{\Omega^2 r_s^2}{2}\right) \tag{6}$$

Equation (6) represents the combined effect of pressure and centrifugal forces.

Note that derivation of the boundary-layer equations (4) from the Navier–Stokes equation (2) was based largely on physical reasoning and an order of magnitude analysis. The same result can be obtained from a more rigorous approach by the use of the method of matched asymptotic expansions.

III. Three-Dimensional Boundary-Layer Flow over a Rotating Blade

The boundary-layer equations determined earlier are applied to flow over a rotating blade. Consider a usual wind turbine blade with a straight leading edge and moderate pitch, which rotates in a uniform

Received 23 July 2002; revision received 27 August 2003; accepted for publication 28 August 2003.

*Professor and Senior Researcher, Department of Fluid Mechanics, P.O. Box 1-24.

†Senior Researcher, Department of Fluid Mechanics, P.O. Box 1-24.

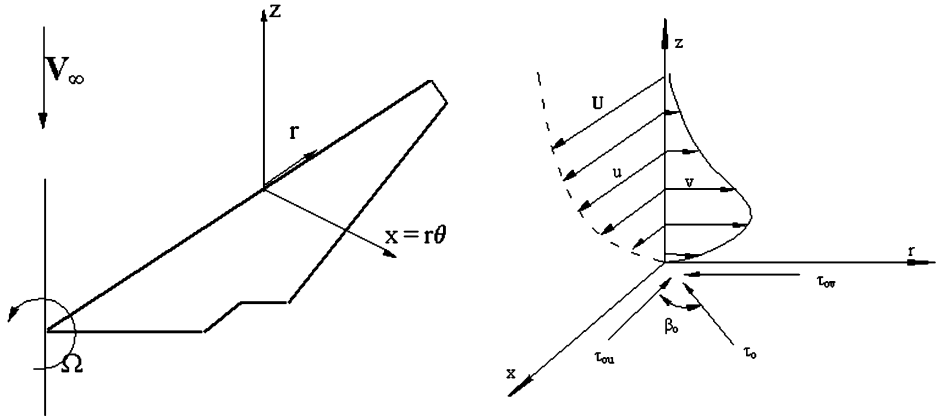

Fig. 1 Cylindrical coordinate system fixed to the rotating blade: nature of chordwise, *u*, and spanwise, *v*, velocity profiles.

stream $\boldsymbol{V}_\infty$ with angular velocity $\boldsymbol{\Omega}$. A cylindrical coordinate system (θ, r, z) fixed to the rotating blade as indicated in Fig. 1 is chosen. With this coordinate system, the continuity equation (3) and the boundary-layer equations (4) can be written as follows.

Continuity:

$$\frac{1}{r}\frac{\partial u}{\partial \theta} + \frac{\partial w}{\partial z} + \frac{\partial v}{\partial r} + \frac{v}{r} = 0 \tag{7}$$

The θ direction momentum:

$$\frac{u}{r}\frac{\partial u}{\partial \theta} + w\frac{\partial u}{\partial z} + v\frac{\partial u}{\partial r} - \frac{v}{r}(2\Omega r - u) = \frac{U}{r}\frac{\partial U}{\partial \theta} + \frac{1}{\rho}\frac{\partial \tau_w}{\partial z} \tag{8}$$

The r direction momentum:

$$\frac{u}{r}\frac{\partial v}{\partial \theta} + w\frac{\partial v}{\partial z} + v\frac{\partial v}{\partial r} + \frac{u}{r}(2\Omega r - u) = U\frac{\partial U}{\partial r} + \frac{1}{\rho}\frac{\partial \tau_v}{\partial z} \tag{9}$$

where u, v, and w are velocity components in θ, r, and z directions, Ω is the angular velocity of the blade, r is the local radius, and τ_u and τ_v are shear stress in the directions of θ and r, respectively. The flow is assumed to be incompressible and steady relative to the blade.

The boundary conditions are at

$$z = 0, \qquad u(x,0) = 0, \qquad v(x,0) = 0, \qquad w(x,0) = 0 \tag{10}$$

as

$$z \to \infty, \qquad u = U(x,r), \qquad v = 0 \tag{11}$$

The typical velocity profiles on a rotating blade look like those of Fig. 1, where β_0 is the angle between the external streamline and the limiting streamline on the blade surface.

The nature and the influence of the main parameters on the three-dimensional boundary-layer behavior are analyzed by use of a local similarity assumption for the special case of a rotating blade of small chord length. Thus, define Blasius parameters

$$\xi = x/c = r\theta/c, \qquad \eta = z\sqrt{U/x\nu} \tag{12}$$

and define

$$\frac{u}{U} = \frac{\partial f}{\partial \eta} = f'(\xi,\eta), \qquad \frac{v}{U} = \frac{\partial g}{\partial \eta} = g'(\xi,\eta) \tag{13}$$

where $U = U(x,r)$ is the inviscid local velocity at $z = 0$, c is the local chord length, and the parameter r/c is inverse proportional with the local solidity.

With ξ and η as independent variables, substitute expressions (12) and (13) into Eqs. (7–9) to obtain

$$f''' + \frac{1}{2}\left(f + 2\xi f_\xi + 2\frac{c}{r}\xi g\right)f'' - \xi f'_\xi f' + \frac{c}{r}\frac{1}{U}\frac{\partial U}{\partial \theta}\xi\left(1 + \frac{1}{2}ff'' - f'^2\right) + \frac{c}{U}\frac{\partial U}{\partial r}\xi\left(\frac{1}{2}f''g - f'g'\right) + \frac{c}{r}\xi g'\left(\frac{2\Omega r}{U} - f'\right) = 0 \tag{14}$$

$$g''' + \frac{1}{2}\left(f + 2\xi f_\xi + 2\frac{c}{r}\xi g\right)g'' - \xi g'_\xi f' + \frac{c}{r}\frac{1}{U}\frac{\partial U}{\partial \theta}\xi\left(\frac{1}{2}fg'' - f'g'\right) + \frac{c}{U}\frac{\partial U}{\partial r}\xi\left(1 + \frac{1}{2}gg'' - g'^2\right) - \frac{c}{r}\xi f'\left(\frac{2\Omega r}{U} - f'\right) = 0 \tag{15}$$

The boundary conditions are

$$\eta = 0, \qquad f(\xi,0) = 0, \qquad f'(\xi,0) = 0, \qquad g(\xi,0) = 0, \qquad g'(\xi,0) = 0 \tag{16}$$

$$\eta \to \infty, \qquad f'(\infty) = 1, \qquad g'(\infty) = 0 \tag{17}$$

where the prime denotes differentiation with respect to η and subscript ξ the differentiation with respect to ξ.

The skin-friction coefficients are given by

$$C_{f,u}\sqrt{Re_x} = 2f''_0, \qquad C_{f,v}\sqrt{Re_x} = 2g''_0 \tag{18}$$

The coupled partial differential equation given by Eqs. (14) and (15) under boundary conditions (16) and (17) are solved numerically by use of Keller's two-point finite difference method with variable step size in combination with Newton's linearization technique (see Ref. 7).

IV. Results and Discussion

The earlier mentioned finite difference scheme was coded, and computations were made for various values of the parameters r/c (local solidity) and X (local relative to rotational velocity ratio). Notice that Rossby number *Ro*, the ratio between inertial forces and Coriolis forces, here is

$$Ro = \frac{U}{\Omega L} = \frac{\sqrt{V_\infty^2 + \Omega^2 r^2}}{\Omega c} = X\frac{r}{c} \tag{19}$$

where X can be interpreted as the ratio between centrifugal forces and Coriolis forces,

$$X = U^2/r\Omega U = \sqrt{1 + (V_\infty/r\Omega)^2}$$

and then r/c is the ratio between centrifugal forces and the inertial forces. If $Ro \gg 1$, the terms due to blade rotation disappear from the equations.

To validate our numerical method, we have compared the results obtained for the inviscid tangential linearly retarded flow [$U = r\Omega X(1 - x/c)$, with $X = 1$], studied by Banks and Gadd,[8] using an integral formulation.

Figure 2 shows the comparison of the separation location (x_s/c) for various values of r/c obtained by the present accurate differential method and the approximate integral methods of Ref. 8. Note that our asymptotic solution ($r/c = \infty$) is identical to that of the well-known Howarth linearly retarded flow. The value of r/c for which the separation condition [$f''(\xi, 0) = 0$)] is never reached is nearly the same as that of Banks and Gadd, $r/c < 0.58$.

Figures 3 and 4 show the effect of the solidity parameter (r/c) on the chordwise skin-friction coefficient and shape parameter. The skin-friction coefficient decreases with r/c, and the shape parameter exhibits larger values for increasing r/c.

This case of linearly retarded external flow on the upper surface of blade can be considered as a triangular-type pressure distribution with reduced pressure peak due to the rotation effect. Then, moving the separation location from the leading edge of blade (12% of chord

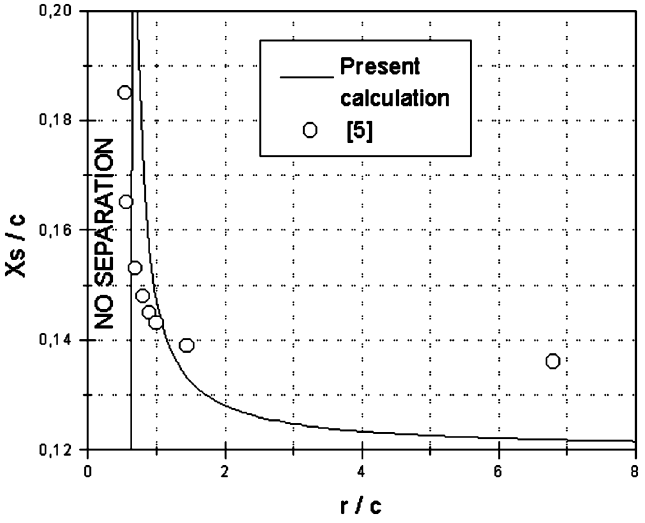

Fig. 2 Downstream variations of separation location (x_s/c) with a radius-to-chord ratio r/c.

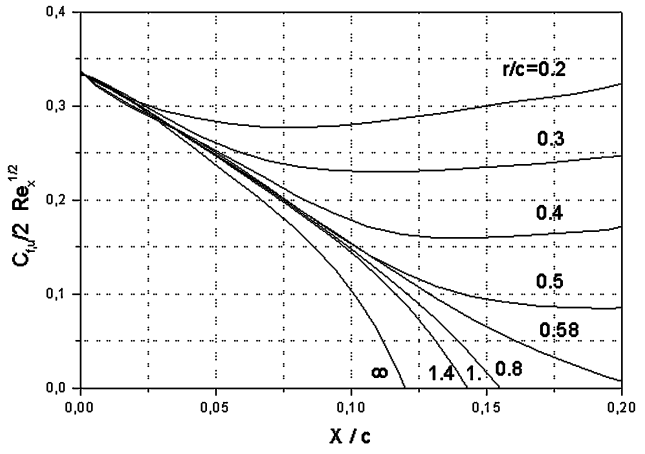

Fig. 3 Downstream variation of skin-friction coefficient ($1/2C_f, uRe_x^{1/2}$) for various ratios r/c.

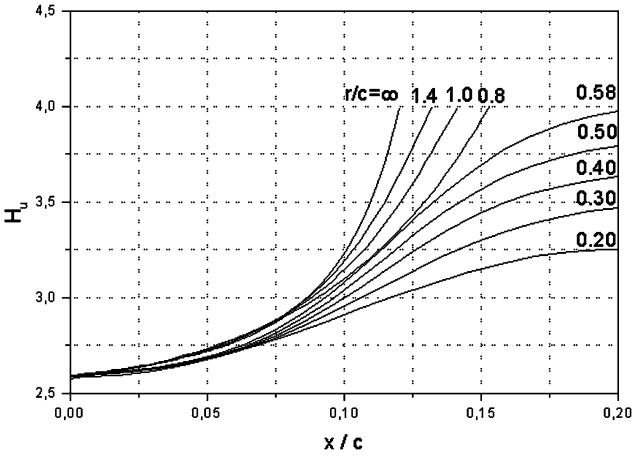

Fig. 4 Downstream variation of shape parameter H_u for various ratios r/c.

for $r/c = \infty$) up to 21% of chord for $r/c = 0.58$ contributes to the beneficial accelerated flow effect in the boundary layer.

The rotation reduces only the global level of pressure on upper surface, without significant influence on pressure gradients. The reduction of the pressure is the contribution of the centrifugal acceleration term, by means of which it is defined as effective pressure. Physically, there is a pumping effect produced by the centrifugal forces that scales with X^2. The important three-dimensional effects are caused mainly by the effect of rotation on the boundary-layer behavior. The Coriolis forces occurring in the boundary-layer flow are the main cause for the stall delay and increased three-dimensional poststall lift coefficients.

V. Conclusions

The present analysis has investigated the influence of the three dimensionality of a rotating blade on the laminar boundary layer that develops from the leading edge on its upper surface, in relation with the widely observed phenomenon of stall delay. It has been proven that the stall delay depends slightly on the reduced pressure effect and mainly on the accelerated boundary-layer flow effect. The pressure distribution mainly is controlled by the rotation parameter X, and Boundary-layer flow is influenced by the radius to local chord ratio, r/c. Both rotational effects become smaller ($X \to 1, r/c \to \infty$) farther outward. This important finding is also reported in Refs. 3 and 5.

The two contributions to separation delay have been discussed. The result shows that the inviscid nature or the explanation of stall delay assumed in Ref. 6 is incorrect, the potential approach being unsuited to describe a phenomenon with complex dynamics.

More work is required to quantify adequately the influence of Reynolds number for a blade at rotating conditions and at high angles of attack.

References

[1]Ronsten, G., "Static Pressure Measurement on a Rotating and a Non-rotating 2.735 m Wind Turbine Blade. Comparison with 2D Calculations," *Journal of Wind Engineering and Industrial Aerodynamics*, Vol. 39, No. 1–3, 1992, pp. 105–118.

[2]Björck, A., Ronsten, G., and Mongomerie, B., "Aerodynamic Section Characteristics of a Rotating and a Non-Rotating 3.375 m Wind Turbine Blade," Aeronautical Research Inst. of Sweden FFA, TN 1995-03, Stockholm, March 1995.

[3]Chaviarropoulos, P. K., and Hansen, M. O. L., Investigating "Three-Dimensional and Rotational Effects on Wind Turbine Blades by Means of a Quasi-3D Navier–Stokes Solver," *Journal of Fluids Engineering*, Vol. 122, 2000, pp. 330–336.

[4]Bosschers, J., "Influence of Blade Rotation on the Sectional Aerodynamics of a Wind Turbine Blade," National Aerospace Lab. NLR, Contract Rept. CR 95290 L, Amsterdam, Sept. 1995.

[5]Du, Z., and Selig, M. S., "The Effect of Rotation on the Boundary Layer of a Wind Turbine Blade," *Renewable Energy*, Vol. 20, No. 2, 2000, pp. 167–181.

[6]Wood, D. H., "A Three-Dimensional Analysis of Stall-Delay on Horizontal-Axis Wind Turbine," *Journal of Wind Engineering and Industrial Aerodynamics*, Vol. 37, 1991, pp. 1–14.
[7]Cebecci, T., *An Engineering Approach to the Calculation of Aerodynamic Flows*, Springer, Berlin, 1999, pp. 51–62.
[8]Banks, W. H. H., and Gaad, G. E., "Delaying Effect of Rotation on Laminar Separation," *AIAA Journal*, Vol. 1, No. 4, 1963, pp. 941, 942.

S. K. Aggarwal
Associate Editor

Microstructured Hydrophobic Skin for Hydrodynamic Drag Reduction

Ashwin K. Balasubramanian,* Adam C. Miller,*
and Othon K. Rediniotis†
Texas A&M University, College Station, Texas 77843

Introduction

An important issue in the development of underwater vehicles and surface ships is devising novel ways to reduce hydrodynamic drag. Drag reduction for small underwater vehicles can alleviate the need for expensive power sources to achieve their specified range and endurance. Large surface and underwater vessels can use drag reduction to extend their ranges, or reduce the amount of fuel consumed or carried. One approach to skin-friction drag reduction involves using a film or discrete layer of air at the wall to take advantage of the greatly lower viscosity of a near-wall gas phase.

Recent attempts to control the production of turbulence near a wall have been reviewed by Bushnell,[1] Bandopadhyay,[2,3] and Gad-el-Hak.[4] The experiments of Bruse et al.[5] show that it is possible to achieve a net drag reduction of 10% with new hybrid surfaces. Jung et al.[6] have numerically shown that a span wise oscillation can lead to 40% reduction on near-wall vorticity fluctuations and drag. Bandopadhyay[7] has used "selective suction and injection" for the control of turbulence in a boundary layer. Wall pressure measurements indicated a slight reduction, which tended to wash out when averaged over more than 500 individual realizations of spectra. Other researchers have studied the slip mechanism in polymer melts and solutions, which cause flow instabilities due to surface interactions.[8]

Here we present findings from our work on a new technology for hydrodynamic drag reduction. It involves a microstructure skin that emulates the surface structure of lotus leaves.[9] A scanning electron microscope picture of the surface is shown in Fig. 1, illustrating the distribution of microstructures on it. It has been observed that beneficial results are obtained if the following conditions are generally met: 1) The nature and character of the surface are selected so that the wetting angle, between a water droplet and the surface, is at a maximum and 2) the contact of the water droplet with the surface has to occur over a minimum area.[10,11] For the surface we tested, when water is deposited on this surface, the combination of the microstructures and the water surface tension traps air between the microstructures. Thus, when water is flowing on the surface, effectively it rides on a layer of air. Because the dynamic viscosity of air (0.000018 kg/m · s) is significantly smaller than that of water (0.001 kg/m · s), the skin friction of the surface and, thus, the hydrodynamic drag are reduced. The objective of this work is to test this artificial surface for quantifying its skin-friction reduction properties. A set of experiments was performed to explore the former and the details are discussed.

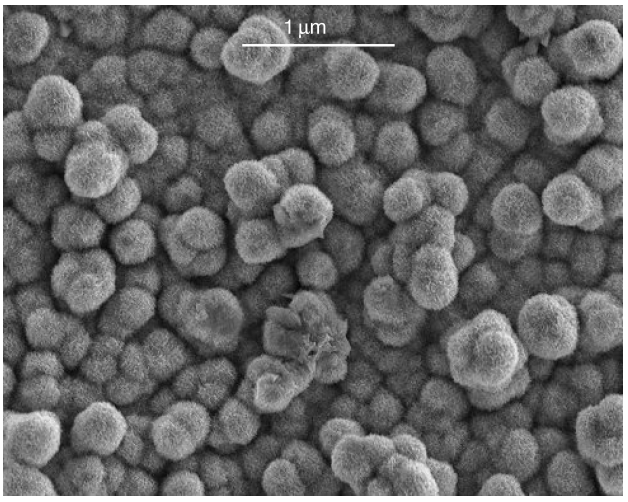

Fig. 1 SEM pictures of microstructure skin surface.

Experimental Setup, Procedures, Uncertainty Analysis, and Discussion of Results

Experiment 1: Flat Plate Model

Particle image velocimetry (PIV) was performed to quantify the effects of the coating/skin on the boundary-layer velocity profile over a flat plate. A flat plate, measuring 55 cm long × 15 cm wide, was tested with and without the coating. The leading edge of the plate was properly shaped to prevent flow separation. In the experiment performed, the flat plate was mounted inside a water tunnel, and the flowfield was seeded with silicon carbide particles, 1.5 μm in diameter. The water-tunnel test section measures 60 cm in length and 15.5 × 19.5 cm in cross section. The water tunnel is capable of operating at speeds up to 470 mm/s. For the current experiment performed, the tunnel was operated at a freestream velocity of 100 mm/s. A laser sheet of power 25 W was used to illuminate the flow. The images were captured using a high-speed Phantom charge-coupled device camera capable of operating at a maximum frame rate of up to 3000 frames per second. The camera was operated at a frame rate of 576 frames per second, and a total of 576 consecutive images were captured. The camera was focused on a 5 × 5 mm area in the boundary layer of the flat plate (view area oriented perpendicular to the plate and parallel to the freestream direction), at a horizontal distance of 44 cm from the leading edge of the plate. Each 512 × 512 pixel image was analyzed to obtain the velocity distribution.

The microstructure skin used in these experiments was generated from two different products, the details of which are as follows: The first product is a Bolta copper foil, which, before processing, behaves like any normal copper foil. The second product is Dynasilan liquid, with which we treated the foil. This liquid is a solution of flourosilane in ethanol. The processing of the foil with the liquid is as follows: A diluted solution (20% vol Dynasilan, 80% vol ethanol) is sprayed on the foil's surface to wet it completely, and the foil is subsequently cured in an oven for one hour at 100°C. After heat treatment, the microstructures on the surface of the foil comprise two different layers, with the microstructures themselves having a height and width of about 300 nm. The surface of the skin was analyzed using an scanning electron microscope (SEM), and Fig. 1 shows the surface of the microstructure skin as viewed through an SEM.

Uncertainty Analysis for Experiment 1

An uncertainty analysis was performed for the PIV measurements using the method described by Kline and McClintock.[12] The

Received 18 June 2002; revision received 1 February 2003; accepted for publication 1 July 2003.

*Graduate Research Assistant, Department of Aerospace Engineering.
†Associate Professor, Department of Aerospace Engineering. Associate Fellow AIAA.